International Journal of Solids and Structures 51 (2014) 2370–2381

Contents lists available at ScienceDirect

International Journal of Solids and Structures

journal homepage: www.elsevier.com/locate/ijsolstr

Numerical simulation of 3D ductile cracks formation using recent improved Lode-dependent plasticity and damage models combined with remeshing

T.-S. Cao *

Mines ParisTech, CEMEF – Center for Material Forming, CNRS UMR 7635, BP 207, 1 rue Claude Daunesse, 06904 Sophia Antipolis Cedex, France

ARTICLE INFO

Article history:
Received 24 October 2013
Received in revised form 28 January 2014
Available online 17 March 2014

Keywords:
Ductile damage
Lode parameter
Remeshing
Cup-cone fracture
Slant fracture

ABSTRACT

Damage to fracture transition has become a popular topic in the ductile fracture scientific community. Indeed, the transition from a damage continuous approach to a discontinuous fracture is not straightforward both from mechanical and numerical points of view. In the present study, a new improved Lode dependent phenomenological coupled damage model is used to investigate the ductile fracture in different mechanical tests. The remeshing and elements erosion techniques are employed to propagate the ductile cracks in 3D models using Forge® finite element code. This code is based on a mixed velocity–pressure formulation using the MINI element $P1+/P1$. In addition, the plasticity behavior is modeled by a Lode-dependent plasticity criterion. Applications to different mechanical tests at different loading configurations, using identified damage model parameters, show good agreement in terms of fracture prediction between experimental and numerical results.

1. Introduction

Damage to fracture transition has become a popular topic in the ductile fracture scientific community. Indeed, the transition from a damage continuous approach to a discontinuous fracture is not straightforward both from mechanical and numerical points of view. Tvergaard and Needleman (1984) first studied numerically the cup-cone fracture formation based on 2D axisymmetric finite element (FE) simulation, by using the GTN model (Gurson, 1977; Tvergaard and Needleman, 1984) and introducing an initial geometrical imperfection. These authors reproduced quite accurately the cup-cone fracture pattern but the use of an initial imperfection was the major limitation of this study. Besson and co-workers (Besson et al., 2001, 2003) used GTN and Rousselier models to study in details the formation of cup-cone and slant fractures as well as the influence of different factors (e.g. mesh design, symmetry, element aspect ratio, constitutive damage parameters etc.) on the numerical fracture surfaces. An indicator was defined by these authors (based on a bifurcation analysis) to detect the zone where strain and damage localization could occur. Based on 2D simulation of plane strain tensile test and 2D axisymmetric tensile test on round bar, the authors concluded that the formation of slant and cup-cone fracture surfaces depends on the constitutive model used as well as mesh size and mesh configuration. The authors showed that, a judicious choice of model constitutive parameters had to be made to obtain the cup-cone fracture (e.g. to obtain the cup-cone, the choice for the critical value of porosity f_c in the GTN model was not a realistic value of the micro-mechanical parameter). Based on experimental results of Bao and Wierzbicki (2004), Teng (2008) carried out the numerical simulation of cup-cone fracture obtained from tensile test on notched round bar and slant fracture obtained with plane strain tensile test. By using the Lemaitre coupled damage model (the 2 parameters version) and 2D FE models with element deletion technique, the author reproduced successfully the 2D slant fracture but the cup-cone fracture was not well captured. Also with the element removal technique, El Khaoulani and Bouchard (2012) used anisotropic mesh adaptation combined with error estimation based on the Lemaitre damage variable and its gradient, to obtain a cup-cone fracture in an axisymmetric tensile test. The main advantage of this method is, starting from a coarse mesh, automatic mesh adaptation and remeshing allow capturing the crack path with sufficient mesh refinement. The CPU time is thus significantly reduced.

Mediavilla and coworkers (Mediavilla et al., 2006a,b) used both coupled (with a regularization technique) and uncoupled damage models combined with a continuous-discontinuous approach as well as a remeshing technique to propagate a crack. More recently,

* Current address: Mines ParisTech, Centre des matériaux, UMR CNRS 7633, 91003 Evry Cedex, France. Tel.: +33 6 68 26 46 11.
E-mail address: trong-son.cao@mines-paristech.fr

http://dx.doi.org/10.1016/j.ijsolstr.2014.03.005
0020-7683/

Nomenclature

C_s, C_{ax}, C_t, C_c, k	material constants in the J_2-J_3 yield criterion
D	Xue damage parameter
E, v	Young's modulus and Poisson's ratio
E_M, σ_M	Young's modulus and flow stress of undamaged material
J_2, J_3	second and third invariants of deviatoric stress tensor
$\dot{\overline{\epsilon}}_p$	equivalent plastic strain rate
ϵ_f	equivalent plastic strain at fracture
$\epsilon_{f0}, p_L, q, k, m, \beta, \gamma, \epsilon_{DX}, D_c$	material constants in the modified Xue damage model
η	stress triaxiality
$\overline{\epsilon}_p$	equivalent plastic strain
$\overline{\sigma}$, q	von Mises equivalent stress
σ_0	flow stress
$\sigma_1, \sigma_2, \sigma_3$	3 principal stresses, $\sigma_1 \geqslant \sigma_2 \geqslant \sigma_3$
$\theta_L, \overline{\theta}$	Lode angle and Lode parameter
$\underset{\sim}{\epsilon}, \underset{\sim}{\epsilon}^p, \underset{\sim}{\epsilon}^e$	total, plastic and elastic strain tensors
$\tilde{p}$	hydrostatic pressure
$w(D)$	weakening function (Xue model)

Feld-Payet et al. (2013) also employed this technique with a non-local formulation to model crack propagation. These studies required remeshing to insert new discrete crack growth. Cracks were inserted along lines where damage was maximum. Seabra and coworkers (Seabra et al., 2013) proposed a similar continuous-discontinuous approach as in Mediavilla et al. (2006a) and Feld-Payet et al. (2013) using the XFEM technique and the non local Lemaitre damage model to simulate cracks propagation without remeshing. Once again, only 2D applications were performed. In addition, many studies among the above-mentioned employed the Lemaitre and GTN damage models, which are stress triaxiality-based, to model damage accumulation process. Several recent studies have proved that the Lemaitre model fails to predict the maximum damage location in shear dominated loadings, for both simple torsion test (Cao et al., 2013b) and shear-dominated forming processes (Cao et al., 2013a). The GTN model is well-known not adapted to predict fracture for shear-dominated loading applications. Recent studies (Xue, 2008; Nahshon and Hutchinson, 2008) proposed different modifications for this model by accounting for the influence of the third deviatoric stress invariant in its formulation. However, these modifications are rather phenomenological, which are not based on micro-mechanical considerations. The use of a suitable damage model, which is capable of capturing the damage localization under different stress states, is essential to obtain an accurate fracture initiation location. In addition to the stress triaxiality, which is the ratio between the mean stress (σ_m) and the von Mises equivalent stress ($\overline{\sigma}$), the Lode parameter has been proved to have important influences on material ductility (e.g. Bai and Wierzbicki, 2008; Barsoum and Faleskog, 2007), thus on damage localization. This parameter is defined by a relation between the second and the third invariants of the deviatoric stress tensor, which helps distinguishing different stress states having a same stress triaxiality ratio. Damage models therefore must account for its influence.

Despite its simplicity, the element removal technique coupled with remeshing is a convenient way to model the damage to fracture transition for 3D configurations. Mesh dependency may deteriorate the stress field computation at the crack tip, which would be particularly problematic for brittle fracture when the crack path is computed based on stress intensity factor. For ductile fracture, the crack path is less sensitive to the local stress field at the crack tip. Fracture can be driven by ductile damage values and the use of the element erosion with a sufficiently fine mesh may conduct to good crack path prediction. In addition, for large strain applications (e.g. uniaxial compression test or metal forming processes) remeshing approach should be used to avoid extreme element distortions and guarantee well-shaped elements once crack is initiated.

In the present study, the formation of cup-cone fracture and slant fracture in tensile tests on notched round bar (NRB) and flat grooved (FG) specimens of a high carbon steel as well as diagonal crack in axisymmetric compression test on an aluminum 2024-T351 is studied. Damage accumulation is calculated using an enhanced Lode dependent damage model initially proposed by Xue (2007a). The remeshing and elements erosion techniques are used to propagate the ductile cracks in 2D axisymmetric and 3D models. With the present approach, neither initial crack (as in Tvergaard and Needleman (1984)) nor discrete crack growth (as in Mediavilla et al. (2006a)) needs to be defined. First, the enhanced Xue damage model is presented, followed by an application in fracture pattern prediction for a compression test on an aluminum, compared with experimental results of Bai and Wierzbicki (2008). In the second section, the tensile tests on NRB and FG specimens are addressed. The strain hardening and damage parameters for the high carbon steel studied were identified from different mechanical tests using J_2 plasticity (Cao et al., 2013a). However, the J_2 plasticity with the hardening law identified fails to describe the plastic behavior in tensile tests on FG specimens. A plasticity model that accounts for the influence of the second and third deviatoric stress invariants is thus employed. For the tensile test on round bar, due to the axisymmetric property of the specimen and loading, a 2D axisymmetric model is used. For the tensile test on flat grooved specimen, the ideal plane strain condition is not fulfilled and a 3D simulation is necessary to capture the crack propagation both through specimen's thickness and specimen's width. The fracture is triggered by critical values of the damage variable and the crack orientation follows the maximum direction of damage. These fracture surfaces are then compared with the experimental results.

2. Models and techniques

2.1. Enhanced Xue model

Xue (2007a) proposed a phenomenological damage model, which is based on the definition of the equivalent fracture strain ϵ_f as a function of hydrostatic pressure (p) and Lode angle (θ_L):

$$\epsilon_f = \epsilon_{f0}\mu_p(p)\mu_\theta(\theta_L), \tag{1}$$

where ϵ_{f0} is the reference fracture strain, which is determined from tension test at constant zero confinement pressure; $\mu_p(p)$ and $\mu_\theta(\theta_L)$ are the pressure-dependent function and the Lode angle-dependent function respectively. Eq. (1) defines a fracture envelope in three-dimensional space of pressure, Lode angle and equivalent strain. Since p and θ_L are orthogonal to each other, they can have separated forms:

$$\mu_p = 1 - q\ln\left(1 - \frac{p}{p_L}\right), \quad \mu_\theta = \gamma + (1-\gamma)\left[\frac{6|\theta_L|}{\pi}\right]^k, \tag{2}$$

where p is the hydrostatic pressure, p_L is the limit pressure (above which damage does not occur), θ_L is the Lode angle, γ is the ratio between fracture strain under shear loading and fracture strain under

uniaxial tension with a same imposed pressure; $k, q > 0$ are material parameters. The Lode angle (Lode, 1925) is defined as:

$$\theta_L = tan^{-1}\left(\frac{1}{\sqrt{3}}\frac{2\sigma_2 - \sigma_1 - \sigma_3}{\sigma_1 - \sigma_3}\right), \tag{3}$$

where $\sigma_1 \geqslant \sigma_2 \geqslant \sigma_3$ are the three principal stresses and $-\pi/6 \leqslant \theta_L \leqslant \pi/6$. This parameter can be normalized to obtain the so-called Lode parameter $\overline{\theta}$ ($-1 \leqslant \overline{\theta} \leqslant 1$), which is defined by:

$$\overline{\theta} = -\frac{6}{\pi}\theta_L. \tag{4}$$

From the expression of μ_p, there exists a cut-off value of pressure where μ_p reduces to zero (so does ϵ_f, which means the material fails immediately):

$$p_{cutoff} = p_L(1 - e^{1/q}) < 0. \tag{5}$$

The scalar damage variable D is used as an internal variable to represent the material degradation. The weakening function $w(D) = 1 - D^\beta$ is adopted to describe the damage effect on the macroscopic strength:

$$\dot{D} = m\left(\frac{\overline{\epsilon}_p}{\epsilon_f(p,\theta_L)}\right)^{m-1}\frac{\dot{\overline{\epsilon}}_p}{\epsilon_f(p,\theta_L)} \quad \text{and} \quad \overline{\sigma} = \left(1 - D^\beta\right)\sigma_M, \tag{6}$$

where β is the weakening exponent; $\overline{\epsilon}_p$ is the equivalent plastic strain; $\epsilon_f(p,\theta_L)$ is the fracture strain, which depends on the current stress state (p,θ_L); σ_M is the flow stress of undamaged material. The coupling between damage and elasticity, e.g. for an uniaxial case, is introduced through: $E = (1 - D^\beta)E_M$, where E_M is Young's modulus of undamaged material.

Based on the studies of Lemaitre (1986), the damage accumulation process is activated above certain threshold defined by a physical parameter (plastic strain or stored energy). For this reason, this observation was adopted for the Xue model by the present author by introducing the strain threshold ϵ_{DX}, from which damage begins to occur, i.e. $\dot{D} = 0$ if $\overline{\epsilon}_p < \epsilon_{DX}$. It should be noted that this parameter might depend on the stress triaxiality level since void nucleation could take place faster and earlier at high stress triaxiality. In the present study, this parameter is supposed constant as in Lemaitre (1986) due to the lack of experimental measurement of real voids evolution to quantify it. At the other end of the damage evolution, when $D = D_c$, a mesocrack is initiated. The damage critical value D_c is another material parameter that needs to be identified. This model is referred to as the enhanced Xue model hereafter. It should be noted that, the original author also used the Xue model to study the flat-to-slant transition fracture mode on a CT specimen (see Xue and Wierzbicki (2009)).

2.2. Finite element model

Implicit finite element (FE) simulations of all experiments are performed using Forge2009®, which is based on a mixed FE formulation of velocity and pressure. In this software, the updated Lagrangian formulation is adopted, which allows using the small strain approach. The local integration of constitutive equations is solved by backward Euler method (return mapping algorithm). Since the mesh is distorted at large deformation, an automatic adaptive remesher (Coupez et al., 2000) allows this software to deal with large strain simulations (e.g. forming processes simulations). The present simulations are carried out with the 3D solver, in which the so-called MINI element ($P1^+/P1$) is used. This linear isoparametric tetrahedron element has a velocity node added at its center, which ensures the stability condition – the Brezzi/Babuska condition of existence and uniqueness of solution. Due to the symmetry property of loading and specimen, one can use only one half or one fourth of the modeled specimen. However, as observed in Besson et al. (2003), using symmetry for crack initiation and propagation simulations can lead to unrealistic higher energy dissipation (e.g. two cracks can be formed instead of one if one quarter of plane strain specimen is used). For this reason, full models of specimens are employed. In addition, the use of the $P1+/P1$ tetrahedral elements favors the mesh generation, which is crucial for automatic remeshing. We implemented the enhanced Xue model through a user subroutine, whose local integration of constitutive equations is presented in the following section.

2.3. Local integration of elasto-plastic damage constitutive equations

In the framework of mixed FE formulation of velocity–pressure (mixed $v-p$), using the $P1+/P1$ tetrahedral elements, the local integration of pressure-dependent plasticity model requires special attention since two resulting pressures can be obtained: one from local integration of behavior (at integration point), another from solving global equilibrium at nodes (see Cao et al. (2013c) for the implementation of the GTN model in this framework). In the following, for a simplification purpose, detailed equations for local integration of elasto-plastic damage model are presented for the incompressible J_2 plasticity.

Isotropic elastic behavior is assumed and the additive strain-rate decomposition is adopted:

$$\underset{\sim}{\sigma} = w(D)\underset{\approx}{D^e} : \underset{\sim}{\epsilon^e}, \tag{7}$$

$$\dot{\underset{\sim}{\epsilon}} = \dot{\underset{\sim}{\epsilon}}^p + \dot{\underset{\sim}{\epsilon}}^e. \tag{8}$$

$w(D)$ is the damage-induced weakening function; $\underset{\approx}{D^e}$ is the elastic continuum tangent modulus of undamaged material; $\dot{\underset{\sim}{\epsilon}}, \dot{\underset{\sim}{\epsilon}}^p$ and $\dot{\underset{\sim}{\epsilon}}^e$ are respectively total, plastic and elastic strain rate tensors. The yield criterion writes:

$$f = \tilde{q} - \sigma_0(\overline{\epsilon}_p) = 0, \tag{9}$$

where σ_0 is the flow stress of material; $\tilde{q} = q/(1 - D^\beta)$ is the effective von Mises equivalent stress (accounting for the coupling between damage and plasticity); $q = \sqrt{3/2(\underset{\sim}{s} : \underset{\sim}{s})}, \underset{\sim}{s}$ is the deviatoric part of the stress tensor $\underset{\sim}{\sigma}$. The plastic flow rule (Prandtl–Reuss) can be obtained from the normality principle:

$$\dot{\underset{\sim}{\epsilon}}^p = \dot{\lambda}\frac{\partial f}{\partial \underset{\sim}{\sigma}} = \frac{3}{2}\frac{\dot{\lambda}}{1 - D^\beta}\frac{\underset{\sim}{s}}{q}, \tag{10}$$

thus, $\dot{\overline{\epsilon}}_p = \frac{\dot{\lambda}}{1-D^\beta}$. Eq. (6) can be written as:

$$\dot{D} = m\left(\frac{\overline{\epsilon}_p}{\epsilon_f}\right)^{m-1}\frac{\dot{\overline{\epsilon}}_p}{\epsilon_f} = m\left(\frac{\overline{\epsilon}_p}{\epsilon_f}\right)^{m-1}\frac{\dot{\lambda}}{(1 - D^\beta)\epsilon_f}. \tag{11}$$

To simplify the writing, the derivations are presented for the case $\epsilon_{DX} = 0$. As in Cao et al. (2013c), the return mapping algorithms (elastic predictor/plastic corrector) together with the Euler implicit scheme was used. For each time step $n+1$, the elastic predictor is obtained by assuming a fully elastic increment:

$$\underset{\sim}{\sigma}^T_{n+1} = \underset{\sim}{\sigma}_n + w(D)_n\underset{\approx}{D^e} : \Delta\underset{\sim}{\epsilon}, \tag{12}$$

where X^T denotes the predictor of the variable X; $\Delta\underset{\sim}{\epsilon}$ is the total strain increment tensor. The subscript $n+1$ means that the variables are evaluated at the time increment $n+1$. It should be noted that, in the context of mixed $v-p$ formulation, the pressure is calculated at nodes by solving global equilibrium equations, the local integration at integration points gives only the deviatoric part of the stress tensor. Therefore, only the deviatoric part ($\underset{\sim}{s}^T_{n+1}$) of the trial stress tensor ($\underset{\sim}{\sigma}^T_{n+1}$) is needed. For each time increment, plastic and damage increments have to be calculated. These two unknowns

are computed simultaneously at each Newton–Raphson iteration by solving the two following equations:

$$\begin{cases} g_1 &= \tilde{q}^T_{n+1} - \frac{3G\Delta\lambda}{1-D_{n+1}} - \sigma_{0(n+1)} = 0, \\ g_2 &= D_{n+1} - D_n - m\left(\frac{\bar{\epsilon}_{p(n)}}{\epsilon_{f(n)}}\right)^{m-1} \frac{\Delta\lambda}{(1-D^{\beta}_{n+1})\epsilon_{f(n)}} = 0, \end{cases} \tag{13}$$

where $\tilde{q}^T_{n+1}$ is the effective, trial equivalent stress: $\tilde{q}^T_{n+1} = \sqrt{3/2(\underset{\sim}{\tilde{s}}^T : \underset{\sim}{\tilde{s}}^T)}$, $\underset{\sim}{\tilde{s}}^T$ is the effective trial deviatoric stress tensor. The term $\tilde{q}^T_{n+1} - \frac{3G\Delta\lambda}{1-D_{n+1}}$ is the plastic correction, where the trial stress state is projected onto the yield surface if it lies outside the yield surface. If the trial stress state is inside the yield surface (i.e. elastic increment), variables update process is straightforward. As in Bouchard et al. (2011), to solve the system (13), two coupling approaches can be used:

- a strong coupling, where two equations of system (13) are solved simultaneously by Newton–Raphson method, which requires the computation of the associated Jacobian matrix. The results at output are: $\Delta\lambda$ and D_{n+1};
- a weak coupling, for which the first equation is firstly solved by using the value D_n instead of D_{n+1} to obtain $\Delta\lambda$; then D_{n+1} is obtained from the second equation, using the computed value of $\Delta\lambda$.

The first method, although it gives more accurate results, is very time consuming; while for the second method, with a sufficient small time step (for a small variation of D in each increment), the results could be equivalent to the first case. In Bourgeon (2009), the author carried out a comparison between weak and strong couplings for the implementation of the Lemaitre model. For a 3D simulation of a tensile test, with a same mesh size and time step, the difference of Lemaitre damage at the specimen center (maximum location of damage) is around 1.8% between the two couplings; while the CPU time for strong coupling is significantly higher (83 min) than the weak coupling (55 min). The global responses (i.e. load–displacement curves) are identical in these two cases. The difference in CPU time increases with the increase of the number of elements (since the number of integration points increases). For the applications presented in this study, since very fine mesh is used, the CPU time is thus significantly higher with the strong coupling. Therefore, the weak coupling has been chosen, with a small time step to ensure the precision of local integration and to accurately control cracks initiation and growth (Section 3). In addition to the internal state variables, consistent tangent moduli can also be obtained. It should be noted that, for the mixed $v-p$ formulation with the use of $P1+/P1$ element, two tangent moduli have to be calculated instead of one: one corresponds to linear velocity (linear tangent modulus) and the other corresponds to the additional velocity node at center of the $P1+/P1$ element ("bubble" tangent modulus) (see Cao et al. (2013c) for detailed computations of tangent moduli for a general pressure-dependent plasticity in the context of mixed $v-p$ formulation).

2.4. Element erosion

When the damage variable in an element reaches the critical value (D_c) at its Gauss point, this element is considered to lose its load bearing capacity. The behavior of this element can be replaced by a soft elastic behavior (as in Li and Zhu (1995) or Besson et al. (2003)). In the present study, an element is removed if its damage value reaches the critical value and the automatic remeshing takes place just after to "repair" the mesh. Crack is propagated by the combination of elements erosion and automatic remeshing.

2.5. Remeshing and variables transfer

The remeshing helps avoiding high distortion elements and tracing cracks path. However, the variables transfer at each remeshing must be well controlled to avoid errors due to the diffusion when projecting field variables from the old mesh to the new one. In Foge2009® with the use of the MINI element, two types of variables transfer are considered: the P_0 variable, which is constant in element and discontinuous when passing from one element to another (i.e. variables at Gauss points, e.g. plastic strain, stress components); and the P_1 variable, which is linear in element and continuous when passing from one element to another (i.e. nodal variables, e.g. velocity, temperature). The terms P_0 transfer and P_1 transfer refer to the transfers of P_0 and P_1 variables respectively. The P_1 transfer is carried out through 2 steps: (1) for each node k of the new mesh, find the element (e') of the old mesh that contains this node; (2) interpolate the nodal value of the nodes of the element e' into the position occupied by the new node k. The P_0 transfer itself is more complex than the P_1 transfer with 4 steps of transfer: (1) in the old mesh, the P_0 variable is extrapolated to nodes; (2) for each node k of the new mesh, find the element (e') of the old mesh containing this node; (3) interpolate the variable P_0 at each node of the element e' of old mesh (which is obtained by the extrapolation in step 1) to the node k; (4) in the new mesh, the variable P_0 is re-interpolated from nodes to the element's center of gravity, and this variable is constant in each element. The extrapolation from the elements to nodes is carried out with classical nodal smoothing by least square method. Illustrations for these two types of variables transfers are presented in Fig. 1.

After remeshing (with remapping of variables) and especially after elements removal and remeshing, the loss of equilibrium state could happen. Several equilibrated remapping methods could be used (e.g. Srikanth and Zabaras, 2000; Brancherie and Villon, 2006) to minimize such a diffusion. However, the problem is generally not critical since it can be handled by considering extra residual forces in the next loading step. In practice, it might lead to an unsatisfied equilibrium state at the beginning of the next increment, which can be reduced by using a small time step.

3. Fracture modeling applications

In this section, three examples of fracture modeling for three different stress states are presented and compared with experimental results. Note that to capture accurately the moment of fracture initiation and the sequence of crack propagation, the loading step should not be too large and the storage step should be controlled in time instead of in displacement.

3.1. Diagonal fracture pattern in uniaxial compression on an aluminum

The simulation of fracture formation in compression test was carried out on the aluminum 2024-T351 using the material parameters presented in Table 1 and the experimental results of Bai and Wierzbicki (2008). For this compression test, the parameters of Xue's model were taken from Xue (2007b, p. 127) : $\epsilon_{f0} = 0.8$, $p_L = 800$ (MPa), $q = 1.5$, $k = 1$, $m = 2$, $\beta = 2$, $\gamma = 0.4$. The strain threshold for damage initiation is $\epsilon_{DX} = 0.06$ and the critical value of damage at fracture is $D_c = 0.9$ (mesh size of 0.1 mm). It should be noted that, the parameters identified by Xue for his model corresponds to $\epsilon_{DX} = 0$. The strain threshold introduced in the present study is small and thus the difference with the original model is negligible. The simulation uses full model of cylinder. The initial diameter of the cylinder is 8 mm and the initial height is 11.25 mm.

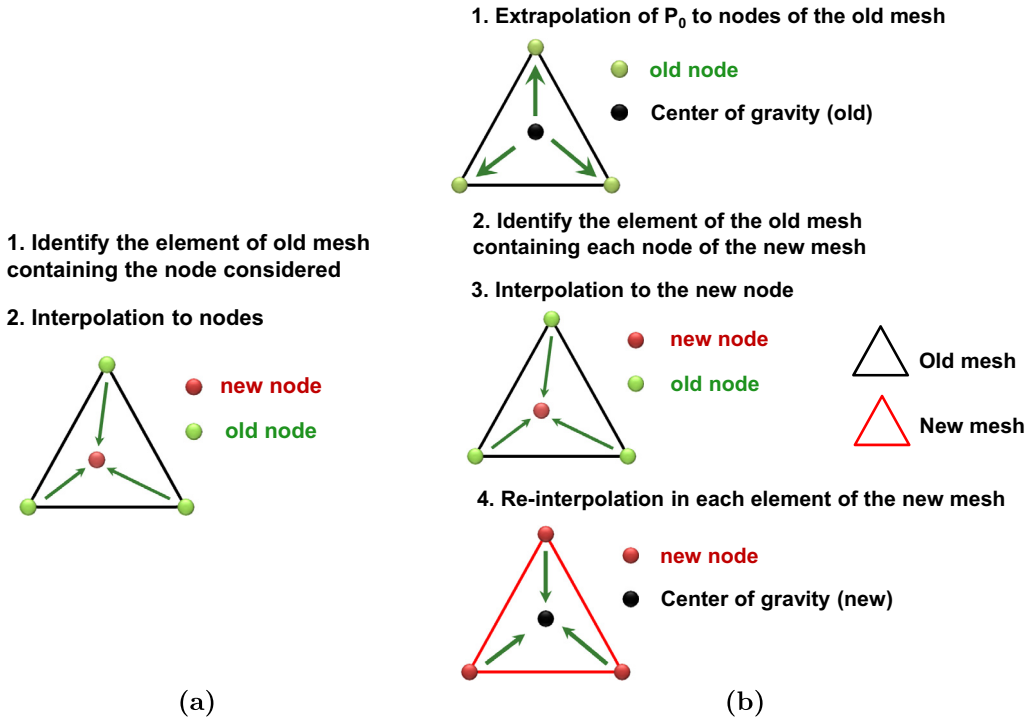

Fig. 1. Illustration of variables transfers in Forge2009®: (a) P_1 variable; (b) P_0 variable.

Table 1
Material properties of aluminum 2024-T351 used for compression simulation. Data were taken from Xue, 2007b (Eq. 10.2 of this document). J_2 plasticity was employed.

Young's modulus (E)	Poisson's ratio (ν)	Flow stress
72400 (MPa)	0.3	$\sigma_0 = 302(1+\bar{\epsilon}_p/0.00387)^{0.173}$

The comparison between the numerical simulation of crack growth and the experimental result of Bai and Wierzbicki (2008) is presented in Fig. 2. The mesh at the end of simulation is also shown in this figure.

As can be observed in Fig. 2 cracks are initiated on the upper surface, then propagate along the maximum damage direction to form the final diagonal fracture pattern. The numerical result is in good agreement with the experimental result regarding the fracture pattern. At the end of the test, diagonal crack is obtained. In addition, tracks on surface are also accurately reproduced. It must be emphasized that the use of a suitable damage model is important to capture such a fracture pattern. The Lemaitre coupled damage model (Lemaitre, 1986) was also tested, but it could not produce this result, crack was initiated in the barreling zone with the Lemaitre model where the stress triaxiality was maximum. The use of remeshing is also crucial since it helps capturing accurately the crack path, and thus reproducing a slant diagonal crack.

3.2. Crack formation in tensile tests on a high carbon steel

For this material, the plasticity and damage models parameters are first identified, then the applications to predict the slant

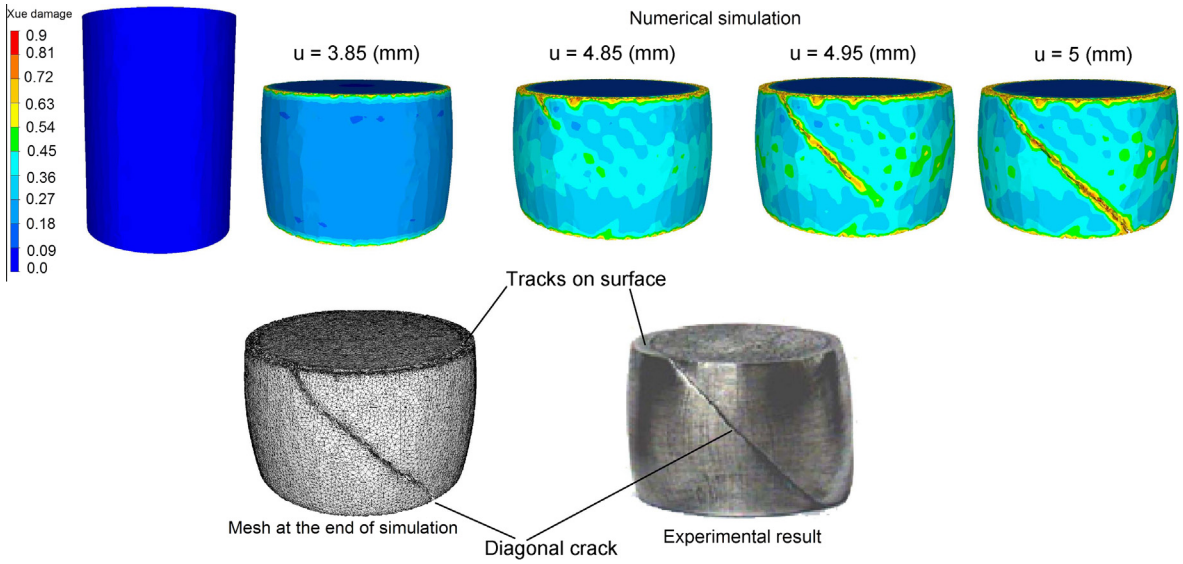

Fig. 2. Comparison between the simulation of crack formation in compression test and the experimental result of Bai and Wierzbicki (2008).

fracture in tensile test on flat grooved specimen and the cup-cone fracture in tensile test on notched round bar specimen are presented.

3.2.1. Material

The material used in the present study is a high carbon steel grade, which presents a fine pearlite structure after a patenting process. All the specimens used in the mechanical tests are extracted from the longitudinal direction of steel rods of maximum diameter of 17 mm. The mechanical property of this steel grade can be considered isotropic at patented state.

3.2.2. Hardening law and plasticity

In this section, the tensile tests on NRB and FG specimens are investigated, using our experimental results on a high carbon steel (Cao et al., 2013a). Seven types of mechanical test are used: three tensile tests on NRB specimens (with notch radii equal to 4, 6 and 9 mm respectively); three tensile tests on FG specimens (with notch radii equal to 2, 5 and 7 mm respectively); one compression test on cylinder specimens. The geometries of the tensile specimens used are shown in Fig. 4(a) and (b). For the compression test, the initial diameter of the cylinder is 8 mm and the height is 11 mm. The objective of the experimental program is to identify constitutive model parameters with a series of tests that covers the whole range of Lode parameter ($\bar{\theta}$ from -1 to 1) and a relatively large range of stress triaxiality (η from $-1/3$ to 0.65). The Lode parameter has been shown to have an important influence on material ductility (e.g. Barsoum and Faleskog, 2007). The configurations of all these tests (i.e. crosshead displacement velocity) were defined in order to have the same order of strain rate, about $1-1.5\ s^{-1}$ (obtained from the preliminary analytical as well as finite elements analyses). All tests were performed at room temperature. For each test, three specimens were used and the results were quite reproducible (<1% of maximum load variation and <4% displacement to fracture variation). For tensile tests, displacement and forces were measured at the driven crosshead. Real displacements of specimen were obtained by eliminating the influence of machine stiffness, both for compression and tensions. In addition, for the flat specimens, due to their small dimensions (1.5 mm of thickness), alignment of specimens in test setup was carefully controlled to avoid induced errors. Fig. 3 represents all the tests in the space of theoretical stress triaxiality and Lode parameter. Note that during these tests, the stress triaxiality and the Lode parameter vary with plastic strain, especially after necking in tensile tests.

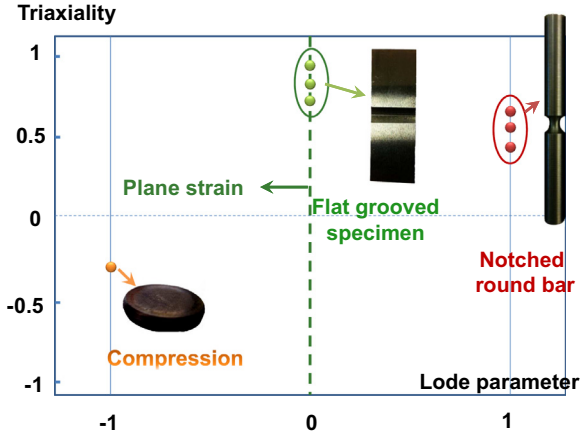

Fig. 3. Representations of macroscopic mechanical tests performed in the space of initial stress triaxiality and Lode parameter.

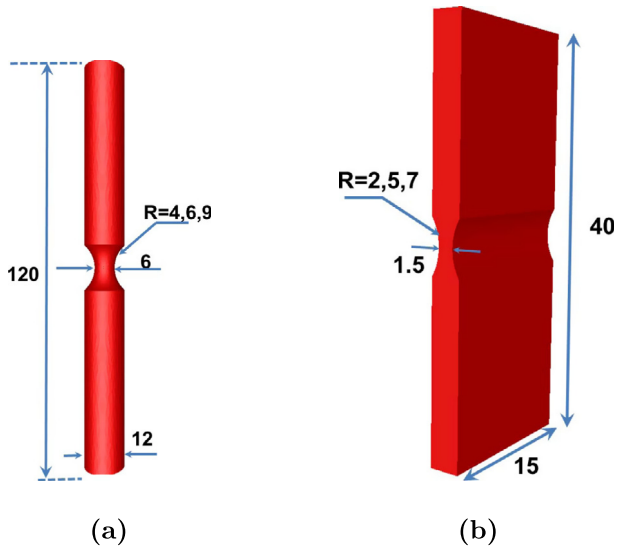

Fig. 4. Geometry and dimensions of the specimens used in tensile tests: (a) notched round bar – NRB specimen, and (b) flat grooved – FG specimen. For each specimen, three notched radii are used. All dimensions are in mm.

In Cao et al. (2013a), the authors identified different isotropic hardening laws (Swift, Ludwik, Voce) but none of them could give correct results in terms of load–displacement curves for both axisymmetric tensile tests on smooth bar and compression tests on cylinder. The Voce law was enhanced to account for the strain hardening at large strain (see Cao et al. (2013a) or Cao (2013) for more details). The elastic–plastic parameters are summarized in Table 2.

Applications of the identified modified Voce hardening law and the J_2 plasticity to the tensile tests on flat grooved specimens show important differences between the experimental load–displacement curves and the numerical ones (see Fig. 6(e)–(g), the green and blue curves). Moreover, anisotropy is not the governing factor for two reasons: firstly, the specimens were machined from a same location and direction of a steel wire; secondly, the anisotropy of this material has been shown to be negligible at the patenting state (see e.g. Massé (2010)). The difference between the two series of tensile tests (axisymmetric specimens and flat grooved specimens) is the stress state that the specimens are subjected to: axisymmetric stress state with axisymmetric specimens ($\bar{\theta}=1, \eta \geqslant 1/3$) and plane strain state with flat specimens ($\bar{\theta}=0, \eta \geqslant 1/\sqrt{3}$) (where η is the stress triaxiality and $\bar{\theta}$ is the Lode parameter). Since ductile damage and fracture often occur after relatively large plastic strain, an accurate plasticity behavior is important to obtain accurate results of damage and fracture. In order to capture the plastic behavior of this material, a plasticity model that depends on the second and the third deviatoric stress invariants (J_2,J_3) developed in Cao (2013) is adopted. The yield criterion writes:

$$\frac{\sqrt{3J_2}}{g(\bar{\theta})} - \sigma_0 = 0, \tag{14}$$

where $g(\bar{\theta})$ is a function of the Lode parameter (or a function of J_2 and J_3); $\sqrt{3J_2}$ is the von Mises equivalent stress. Inspiring from

Table 2
Material properties of the high carbon steel used for tensile tests simulations (Cao et al., 2013a).

E	ν	Flow stress
210,000 (MPa)	0.3	$\sigma_0 = 601.15 + (512.05 + 100\bar{\epsilon}_p)(1 - exp(-37\bar{\epsilon}_p))$

the plasticity model proposed by Bai and Wierzbicki (2008), $g(\overline{\theta})$ is taken as a polynomial function of $\overline{\theta}$:

$$g(\overline{\theta}) = C_s + (C_{ax} - C_s)\left(\overline{\theta}^2 - \frac{\overline{\theta}^{2k}}{2k}\right), \tag{15}$$

where $C_s = g(\overline{\theta}=0), C_{ax} = \begin{cases} C_t, & if \quad \overline{\theta} \geqslant 0 \\ C_c, & if \quad \overline{\theta} < 0 \end{cases}$. The high order power term $\frac{\overline{\theta}^{2k}}{2k}$ was introduced to make the yield surface smooth and differentiable with respect to Lode angle around $\overline{\theta} = \pm 1$. If k is significantly high, $C_t \approx g\ (\overline{\theta}=1)$ and $C_c \approx g(\overline{\theta}=-1)$. $k = 30$ have been fixed for the present applications. The convexity of the yield surface is assured when $\frac{\sqrt{3}}{2} \leqslant \frac{C_s}{C_{ax}} \leqslant 1$. The plots of the J_2-J_3 yield surfaces in the principal stress space and for plane stress condition are shown in Fig. 5(a) and (b), which show that the J_2-J_3 yield surface used can be considered as an intermediate of the von Mises and the Tresca ones (Fig. 5(b)).

Since the modified Voce hardening law is validated for the axisymmetric tensile tests, the parameter C_t is chosen equal to unity. Two additional parameters C_s and C_c need to be identified. The identification of these parameters is based on the multi-objectives optimization by inverse analysis, which aims at minimizing the discrepancy between numerical and experimental load–displacement curves of the three tensile tests on FG specimens. The results give $C_c = 0.95, C_s = 0.87$ and a slight modification of the modified Voce hardening law: $\sigma_0 = 601.15 + (562.05 + 100\overline{\epsilon}_p)\ (1 - exp\ (-37\overline{\epsilon}_p))$. The comparison between experimental and numerical curves is shown in Fig. 6 for all seven tests, which shows the validity of the proposed plasticity criterion. This plasticity criterion and the identified hardening model are used for the simulations of fracture. Two tests are retained for fracture simulations: the tensile test on FG-R7 specimen (flat grooved specimen with the notch radius equal to 7 mm) and the tensile test on NRB-R6 specimen (notched round bar specimen with the notch radius equal to 6 mm).

3.2.3. Slant fracture in tensile test on FG specimen

Under plane strain loading, conditions for the plastic flow localization were extensively investigated (see e.g. Tvergaard (1982) or the reviews of Tvergaard (1990) and Benzerga and Leblond, 2010). In numerical simulations, the presence of a vertex in the yield surface could favor the macroscopic localization prior to fracture (Tvergaard, 1990). For the present $J_2 - J_3$ plasticity model, a high order term is added to obtain a smooth yield surface, thus avoid such a perturbation (i.e. the vertex) on the plastic flow.

In the literature, the simulation of crack formation in tensile on flat specimen (plane strain stress state) was often done in 2D. However, in some cases as in the present experimental result, the plane strain state is not fulfilled and lateral necking of specimen at the end of the experiment can be observed (see Fig. 7(a)). Moreover, with 2D model, only through thickness crack propagation can be observed and one does not have a 3D view of crack propagation through the width of the specimen. In this section, the 3D crack formation in the tensile test on FG-R7 specimen is investigated.

The used parameters of the enhanced Xue model are: $\epsilon_{f0} = 0.6$, $p_L = 1735$ (MPa), $q = 0.236$, $k = 1$, $m = 2$, $\beta = 2$, $\gamma = 1.1$, $\epsilon_{DX} = 0.054$, $D_c = 0.6$. The mesh size in the gauge section is 0.035 mm (see Fig. 9). Identification of these parameters was detailed in Cao et al. (2013a). It was based on the axisymmetric compression and tensile tests as well as torsion test. The identification was based on the softening effect of damage (for the tensile test on round bar and the compression test). In addition, the resulting error was evaluated from the discrepancy between numerical and experimental displacements to fracture (the numerical displacement to fracture is the displacement necessary for which the maximum value of damage variable reaches it critical value D_c). The damage variable was calculated from ϵ_f, which is the function of μ_p and μ_θ (Eq. (11)). The identification procedure was then decoupled into two steps: identification of the pressure-dependent function μ_p with the series of tensile tests on RB and NRB (in which the Lode angle-dependent function μ_θ varies slightly, $\theta_L \approx -\pi/6$ during these tests), and identification of μ_θ with torsion test (in which $\mu_p \approx 1$ since $p \approx 0$). Xue proposed $k = 1$ and $m = 2$ and these values were kept for the multi-objective optimization by inverse analysis. There was thus one parameter (γ) in μ_θ to be identified from the torsion test. The evolution strategy technique has been adopted for the optimization process. All details about the identification procedure can be found in Cao et al. (2013a).

The experimental result of cracked specimen at the end of the test is represented in Fig. 7(a), showing a slant surface, while the numerical one is shown in Fig. 7(b). They are in good agreement with each other. Moreover, these figures also reveal a lateral necking through width direction (see red arrows in these figures), which suggest that the plane strain condition is not fulfilled. In

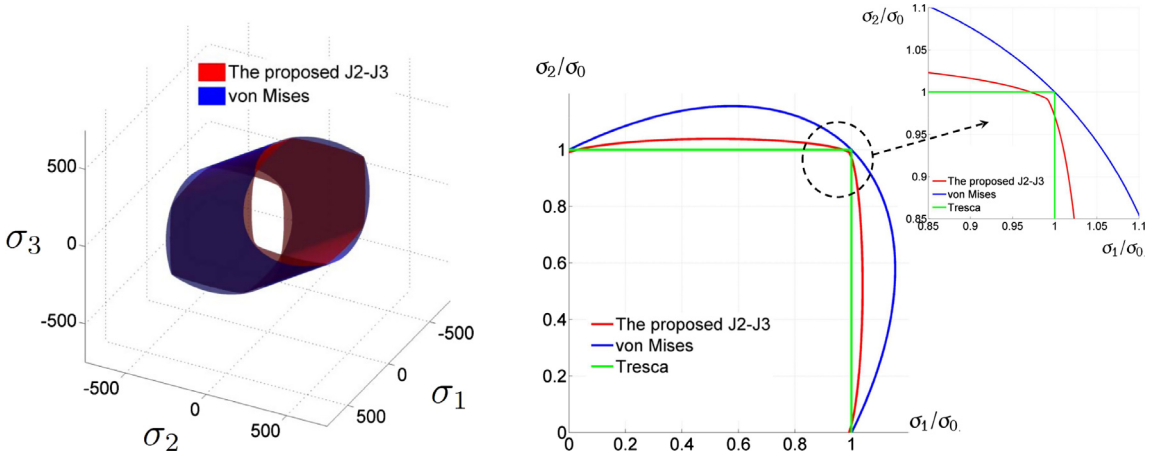

(a) *Principal stress space.* (b) *Plane stress space. The zoomed picture shows yield surfaces near* $\overline{\theta} = 1$.

Fig. 5. Comparison of yield surfaces: (a) in principal stress space (von Mises and the proposed J_2-J_3); (b) plane stress condition (von Mises, Tresca and the proposed J_2-J_3). The J_2-J_3 surface is obtained with $C_c = C_t = 1, C_s = 0.9$ and $k = 6$.

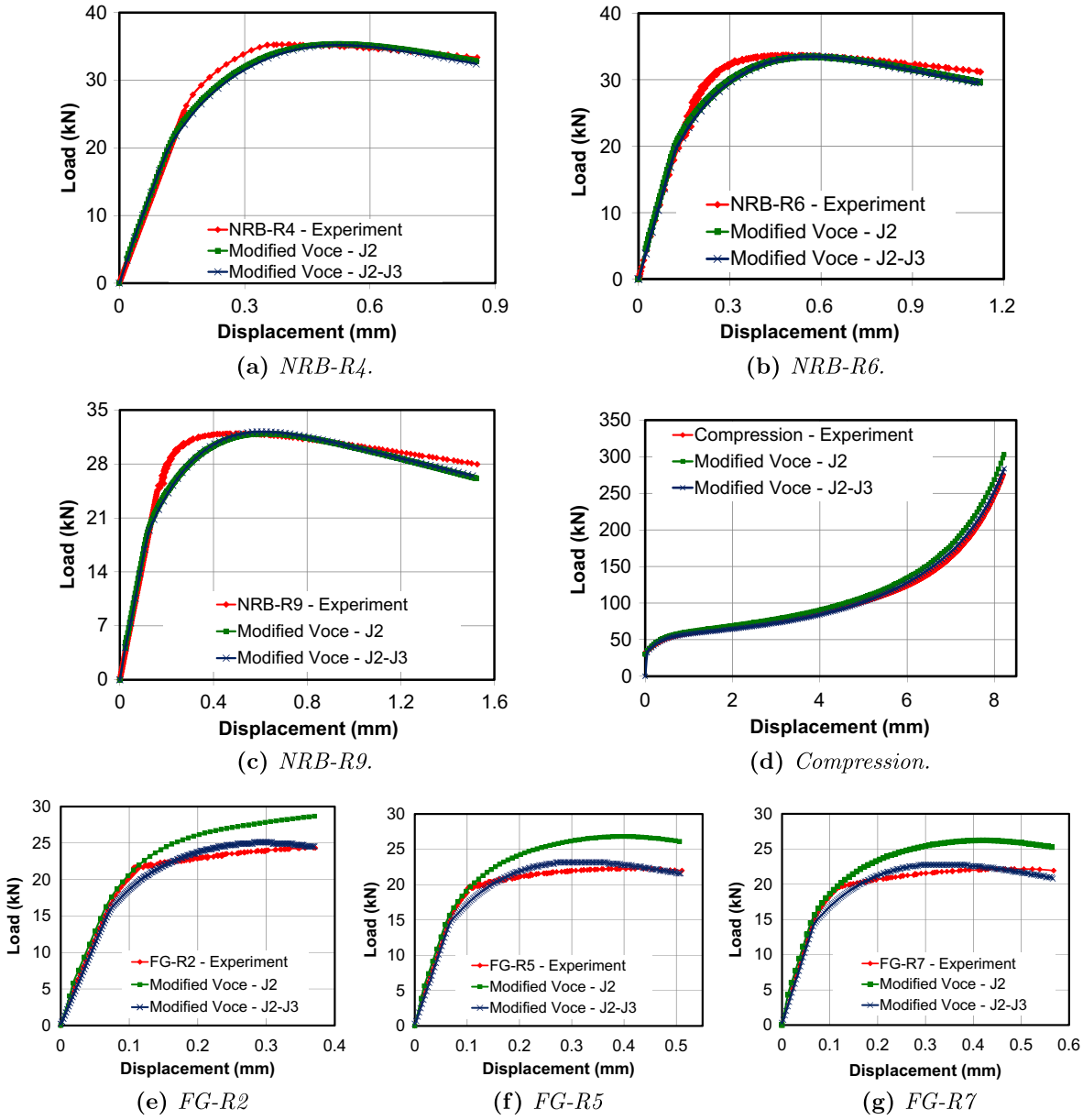

Fig. 6. Comparison of load–displacement curves of mechanical tests using the implemented J_2–J_3 plasticity criterion and its identified parameters combined with the modified Voce hardening law. (For interpretation of the references to colour in this figure caption, the reader is referred to the web version of this article.)

order to understand the crack initiation and growth, the sequence of crack formation is represented in Fig. 8. The meshes at different instants are also shown in Fig. 9.

As observed in Fig. 8, crack initiates at the specimen center ($u = 0.465$ mm), then propagates through thickness following a direction about 45° to the loading direction ($u = 0.477$ mm). Then, the crack propagates outward (through width) to totally separate the specimen ($u = 0.566$ mm). This sequence of crack propagation can only be obtained with 3D model. The numerical result of fracture surface is consistent with the experimental one.

3.2.4. Cup-cone fracture in tensile test on notched round bar specimen

The fracture observed in the tensile tests on round bars or NRB is often the cup-cone fracture, where crack initiates at the specimen center then propagates outward in the first stage (flat mode). A shear lip forms at the circumferential edge of the outer surface (slant mode) and a cup-cone fracture is obtained. The tensile test on NRB-R6 is investigated, using the experimental results on the high carbon steel. The specimen geometry is presented in Fig. 4(a). The same set of parameters as in Section 3.2.3 is used. The comparison between the experimental and numerical fracture surfaces is shown in Fig. 10.

From the experimental result, two zones can be distinguished, one corresponds to the flat fracture mode at the specimen center, and the other corresponds to the slant fracture mode observed near the circumference. It can be captured by the numerical simulation. Fig. 10 shows that the numerical simulation with the enhanced Xue model and identified parameters gives relatively correct result in terms of crack formation prediction. The sequence of crack formation is represented in Fig. 11, which is also consistent with the experimental result discussed above.

4. Discussions

4.1. On the role of damage models

The three above test cases show the efficiency of the present approach to model cracks initiation and growth in crack-free ductile

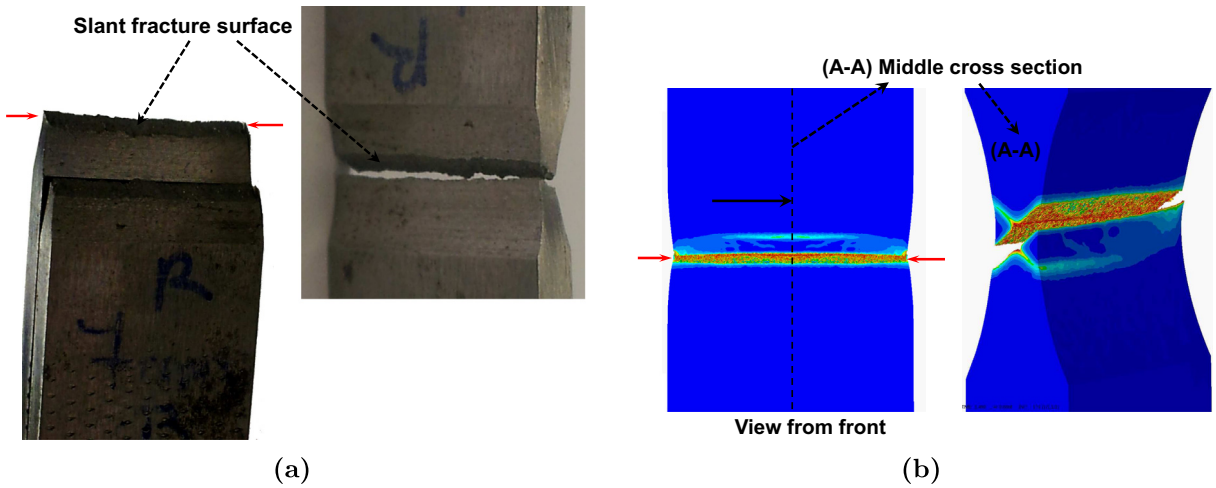

Fig. 7. Comparison between the experimental and numerical fractured surfaces of FG-R7 specimen: (a) experimental slant fractured surface and lateral necking observed; and (b) the left figure shows the lateral "necking" and the right figure shows the view from the middle cross section obtained with numerical simulations.

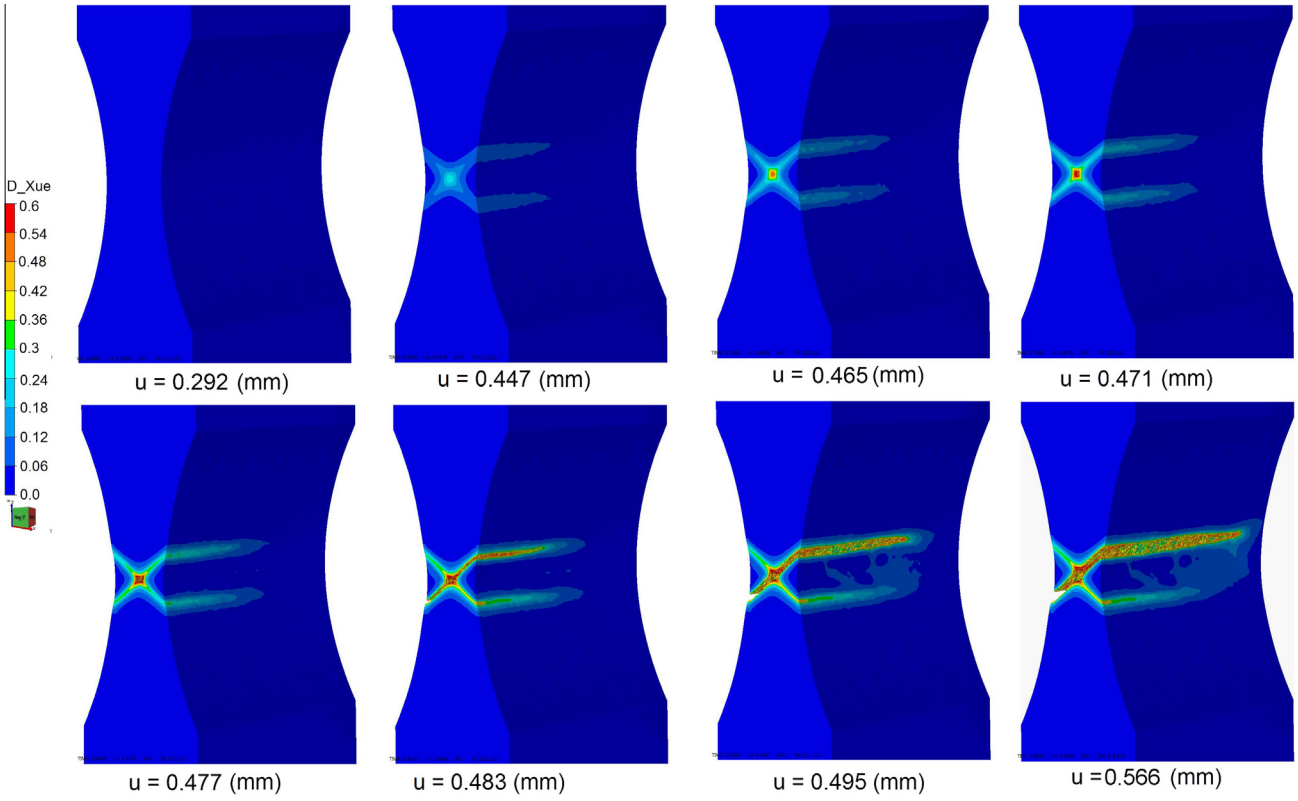

Fig. 8. Sequence of crack initiation and growth in tensile test on FG specimen represented on a half of the specimen.

solids subjected to different types of loading. It should be emphasized that all constitutive and material parameters used were identified from mechanical tests at different loading configurations.

In general, damage models can be classified into three groups: uncoupled phenomenological models (e.g. Bai and Wierzbicki, 2008; Modified Mohr–Coulomb – MMC Bai and Wierzbicki, 2010; Dunand and Mohr, 2010); coupled phenomenological models (e.g. Lemaitre model in the Continuum Damage Mechanics framework, or Xue phenomenological model); and micro-mechanically-based models (e.g. GTN or Gologanu–Leblond–Devaux models). In the present study, phenomenological coupled Xue model is selected. This choice, however, is not an arbitrary choice. The Xue model accounts for the influence of both stress triaxiality and Lode parameter, which are two important variables on damage accumulation. Moreover, material softening due to damage accumulation can also be captured through a weakening function. Several modifications have been adopted for this model to account for the damage threshold defined by a critical equivalent plastic strain. Uncoupled models (Bai and Wierzbicki and MMC) were also tested but they could only reproduce the slant crack in plane strain tensile tests and failed in the two other cases. The use of micro-mechanical models (e.g. GTN as in Besson et al. (2001)) or coupled models in the continuum damage mechanics framework (e.g. Lemaitre as in El Khaoulani and Bouchard (2012)) might also be possible to

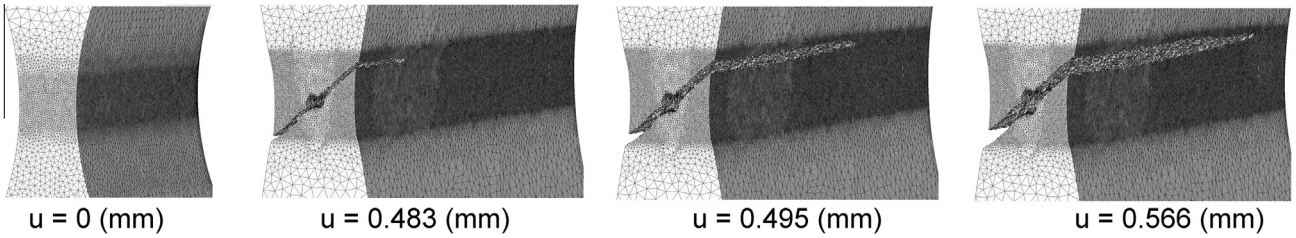

Fig. 9. Meshes at different instants.

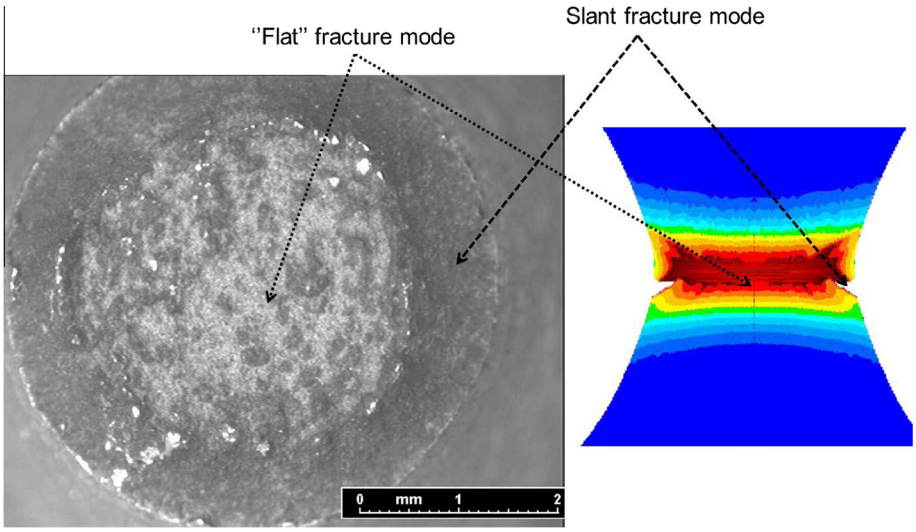

Fig. 10. Comparison between the experimental (left) and the numerical (right) fracture surfaces of NRB-R6 tensile specimen (for the numerical result, view is from middle vertical cross section).

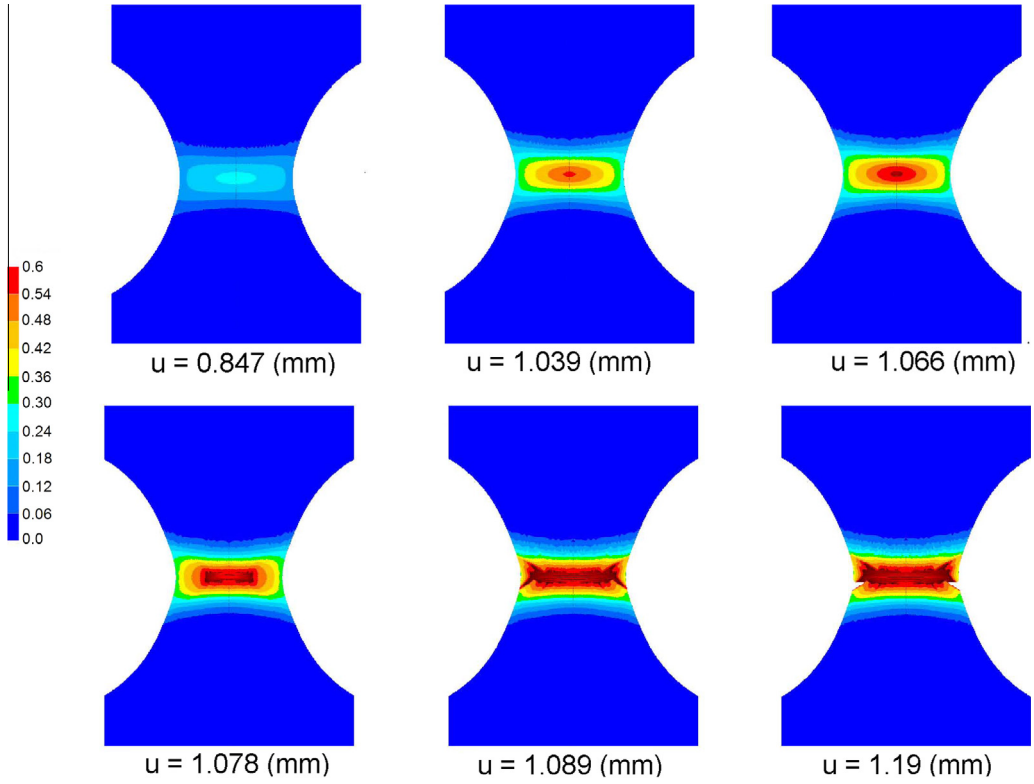

Fig. 11. Sequence of crack initiation and growth in tensile test on NRB-R6 specimen represented on a half of the specimen.

produce the cup-cone or slant fractures in tensile tests on axisymmetric and flat specimens (at high stress triaxiality). However, these models have not been shown to be capable of capturing crack growth at low stress triaxiality application (e.g. slant diagonal crack in the upsetting test). This shortcoming can be overcome by adding a Lode-dependent term in these classical models to better capture damage accumulation at both high and low stress triaxialities (as done by Nahshon and Hutchinson (2008) and Xue (2008) for the GTN model and by e.g. Cao et al. (2014a) for the Lemaitre model). These modified models would be tested in future studies to simulate crack formation at low stress triaxiality. However, by applying these modifications, the modified GTN models are no longer micro-mechanical model, but rather phenomenological one. The use of a phenomenological approach, as presented here, is fully justified even though it cannot deliver much insight into the physics.

In addition, regarding micro-mechanical models, for reliable application results, models parameters have to calibrated from microscopic observations since they are based on microscopic consideration (see e.g. Cao et al. (2014b) for a recent study on the identification of the GTN model modified by Xue by using combined macroscopic mechanical tests and in situ X-ray micro-tomography observations). The calibration procedure is thus costly. Moreover, even if physical based parameters are identified, the use of such a model (e.g. GTN) does not always guarantee correct fracture modes. As indicated in Besson et al. (2001), the use of the value of their identified critical porosity $f_c = 0.005$ (which defines the onset of coalescence) prohibited the formation of cup-cone fracture. Later, in Besson et al. (2003), the authors reported similar results for fracture prediction in plane strain bars under tension. They found that, a judicious choice of $f_c = 0.01$ favored the flat fracture. These results suggest that, even for high stress triaxiality applications, the GTN has some, but not all ingredients to model cup-cone and plane strain fracture (see detailed discussion in Benzerga and Leblond (2010)). In addition to the choice of a suitable damage models, attention has to be paid to numerical techniques, which are detailed in the following.

4.2. On the role of numerical techniques

As shown in the early work of Tvergaard and Needleman (1984), mesh designs (and mesh size in particular) play an important role in fracture prediction. If no mesh regularization technique is used (e.g. non local model), the results depend strongly on mesh size: a smaller mesh size leads to a higher damage value. Apart from this problem, mesh design is also a crucial factor to describe the crack path. In Tvergaard and Needleman (1984), a zig-zag growth was obtained form tensile test on axisymmetric specimen, which is most likely due to symmetry assumption. In addition, the use of symmetry should be avoided due to resulting non-physical high dissipation energy (see Besson et al., 2003). Elements aspect ratios were shown to have important roles if remeshing was not used. Choosing a suitable initial aspect ratios helps avoiding extreme element distortion when crack is initiated (Besson et al., 2003). In the present study, since remeshing is used to assure well-shaped elements, there is thus no particular attention to be paid on the choice of initial aspect ratios.

Regarding numerical technique, in El Khaoulani and Bouchard (2012), the authors used anisotropic mesh adaptation and the Lemaitre model to model the cup-cone fracture. They also reported that without automatic mesh adaptation, a flat fracture model was obtained instead of a cup-cone mode. Similar results are obtained in the present study. Without automatic remeshing, 3D diagonal cracks in upsetting test cannot be captured accurately.

In summarizing, in order to successfully capture cracks formation in ductile solids subjected to complex loadings, the following requirements should be satisfied: (1) the use of a suitable coupled damage model that can capture damage localization for both high and low stress triaxialities; (2) models parameters should be identified from mechanical tests at different loading configurations; and (3) numerical techniques, such as automatic remeshing coupled with accurate remapping, should be used. The main advantage of the present approach is the continuous control of damage, from damage accumulation to crack initiation and growth. Neither predefined crack path, nor discrete crack have to be introduced. However, the present method still suffers several limitations. A local formulation has been used, which leads to mesh size dependent solutions, and there is no method used to control fracture energy. In addition, since adaptive remeshing has not been developed, predefined fine mesh has to be used in the location of interest, the CPU time is thus higher than that with adaptive remeshing (as in El Khaoulani and Bouchard (2012)). These problems might be subjects of future studies.

5. Closure remarks

In the present study, an enhanced Xue coupled damage model combined with element erosion and remeshing techniques are used to model the crack initiation and growth for different mechanical tests. Main results are summarized as:

- First, formulations and the implementation of the enhanced Xue model in a framework of mixed velocity–pressure FE formulation using the $P1 + /P1$ element are presented. Several enhancements are proposed, namely the damage threshold defined by a critical value of equivalent plastic strain and the use of a critical value of damage to define the crack initiation (which depends on mesh size since non local formulation is not used).
- Applications to different loading configurations are then presented. Except for the compression test where the experimental result is taken from the results of Bai and Wierzbicki, the two other tests (tensions on axisymmetric and flat specimens) are compared with our experimental results on a high carbon steel, using real material parameters identified. A J_2-J_3 plasticity criterion is developed and applied to this material.
- The proposed method predicts accurately different fracture modes for different loading configurations: diagonal crack in compression, slant mode in tensile test on FG specimen and cup-cone mode in tensile test on NRB specimen. There is no need to define the crack path because it is based on elements removal and remeshing. Moreover, this method is continuous, which means that one can control the whole process, from damage growth and crack initiation, to crack propagation. It is worth noting that the use of a suitable damage model as in the present study is important to capture the damage distribution and localization and so reproduce the fracture pattern. However, the main drawbacks of this method are that the fracture energy cannot be accurately controlled and the solution depends on mesh size since no regularization technique has been employed. Moreover, fine mesh zones have to be predefined to capture accurately the fracture, where the use of an automatic mesh adaptation is of interest to reduce the computational cost. These problems might be subjects of future studies. Nevertheless, these validations compared with experimental results show the efficiency of such a continuous approach to model 3D crack growth without the need of introducing artificial instabilities.

Acknowledgments

The author would like to acknowledge the helpful suggestions and fruitful discussions from Pierre-Olivier Bouchard and Pierre

Montmitonnet at Center for material forming – Sophia Antipolis, France. The financial support from ArcelorMittal, Cezus-Areva and Ugitech via the METAL project is appreciated.

References

Bai, Y., Wierzbicki, T., 2008. A new model of metal plasticity and fracture with pressure and Lode dependence. Int. J. Plasticity 24 (6), 1071–1096.

Bai, Y., Wierzbicki, T., 2010. Application of extended Mohr–Coulomb criterion to ductile fracture. Int. J. Fract. 161 (1), 1–20.

Bao, Y., Wierzbicki, T., 2004. A comparative study on various ductile crack formation criteria. J. Eng. Mater. Technol. 126 (3), 314–324.

Barsoum, I., Faleskog, J., 2007. Rupture mechanisms in combined tension and shear–experiments. Int. J. Solids Struct. 44 (6), 1768–1786.

Benzerga, A.A., Leblond, J.-B., 2010. Ductile fracture by void growth to coalescence. Advances in Applied Mechanics, vol. 44. Elsevier, pp. 169–305.

Besson, J., Steglich, D., Brocks, W., 2001. Modeling of crack growth in round bars and plane strain specimens. Int. J. Solids Struct. 38 (46–47), 8259–8284.

Besson, J., Steglich, D., Brocks, W., 2003. Modeling of plane strain ductile rupture. Int. J. Plasticity 19 (10), 1517–1541.

Bouchard, P.-O., Bourgeon, L., Fayolle, S., Mocellin, K., 2011. An enhanced Lemaitre model formulation for materials processing damage computation. Int. J. Mater. Form. 4, 299–315.

Bourgeon, L., 2009. Etude et Modélisation des Mécanismes d'Endommagement en Forge à Froid (Ph.D. thesis). School Ecole nationale Supérieure des Mines de Paris (in French).

Brancherie, D., Villon, P., 2006. Diffuse approximation for field transfer in non linear mechanics. Eur. J. Comput. Mech. (Revue Européenne de Mécanique Numérique) 15 (5), 571–587.

Cao, T.-S., 2013. Modeling Ductile Damage for Complex Loading Paths (Ph.D. thesis). School Ecole Nationale Supérieure des Mines de Paris.

Cao, T.-S., Bobadilla, C., Montmitonnet, P., Bouchard, P.-O., 2013a. On the development and identification of phenomenological damage models – application to industrial wire drawing and rolling processes. Key Eng. Mater 554–557, 213–226.

Cao, T.-S., Gaillac, A., Montmitonnet, P., Bouchard, P.-O., 2013b. Identification methodology and comparison of phenomenological ductile damage models via hybrid numerical-experimental analysis of fracture experiments conducted on a zirconium alloy. Int. J. Solids Struct. 50 (24), 3984–3999.

Cao, T.-S., Montmitonnet, P., Bouchard, P.-O., 2013c. A detailed description of the Gurson–Tvergaard–Needleman model within a mixed velocity-pressure finite element formulation. Int. J. Numer. Methods Eng. 96 (9), 561–583.

Cao, T.-S., Gachet, J.-M., Montmitonnet, P., Bouchard, P.-O., 2014a. A Lode-dependent enhanced Lemaitre model for ductile fracture prediction at low stress triaxiality (submitted for publication).

Cao, T.-S., Maire, E., Verdu, C., Bobadilla, C., Lasne, P., Montmitonnet, P., Bouchard, P.-O., 2014b. Characterization of ductile damage for a high carbon steel using 3D X-ray micro-tomography and mechanical tests – application to the identification of a shear modified GTN model. Comput. Mater. Sci. 84, 175–187.

Coupez, T., Digonnet, H., Ducloux, R., 2000. Parallel meshing and remeshing. Appl. Math. Modell 25 (2), 153–175.

Dunand, M., Mohr, D., 2010. Hybrid experimental–numerical analysis of basic ductile fracture experiments for sheet metals. Int. J. Solids Struct. 47 (9), 1130–1143.

El Khaoulani, R., Bouchard, P., 2012. An anisotropic mesh adaptation strategy for damage and failure in ductile materials. Finite Elem. Anal. Des. 59, 1–10.

Feld-Payet, S., Chiaruttini, V., Feyel, F., 2013. A crack insertion strategy based on a gradient-type criterion and local remeshing. In: Conference Proceedings – CFRAC 2013, 1, Repro Fetterle, Prague, Czech Republic, vol. 96.

Gurson, A.L., 1977. Continuum theory of ductile rupture by void nucleation and growth: Part I-yield criteria and flow rules for porous ductile media. J. Eng. Mater. Technol. 99 (1), 2–15.

Lemaitre, J., 1986. Local approach of fracture. Eng. Fract. Mech. 25 (5–6), 523–537.

Li, G.-C., Zhu, C., 1995. Formation of shear bands in plane sheet. Int. J. Plasticity 11 (5), 605–622.

Lode, W., 1925. Versuche über den einfluder mittleren hauptspannung auf die flie grenze. Zeit. Angew. Math. Mech. 5, 142–144.

T. Massé, T., 2010. Study and Optimization of High Carbon Steel Flat Wires (Ph.D. thesis). School Ecole Nationale Supérieure des Mines de Paris.

Mediavilla, J., Peerlings, R., Geers, M., 2006a. Discrete crack modelling of ductile fracture driven by nonlocal softening plasticity. Int. J. Numer. Methods Eng. 66 (4), 661–688.

Mediavilla, J., Peerlings, R., Geers, M., 2006b. A robust and consistent remeshing-transfer operator for ductile fracture simulations. Comput. Struct. 84 (8–9), 604–623.

Nahshon, K., Hutchinson, J., 2008. Modification of the Gurson model for shear failure. Eur. J. Mech. – A/Solids 27 (1), 1–17.

Seabra, M.R.R., Sustaric, P., Cesar de Sa, J.M.A., Rodic, T., 2013. Damage driven crack initiation and propagation in ductile metals using XFEM. Comput. Mech. 52 (1), 161–179.

Srikanth, A., Zabaras, N., 2000. Shape optimization and preform design in metal forming processes. Comput. Methods Appl. Mech. Eng. 190 (13–14), 1859–1901.

Teng, X., 2008. Numerical prediction of slant fracture with continuum damage mechanics. Eng. Fract. Mech. 75 (8), 2020–2041.

Tvergaard, V., 1982. On localization in ductile materials containing spherical voids. International Journal of Fracture, 0376-9429 18 (4), 237–252.

Tvergaard, V., 1990. Material failure by void growth to coalescence. Adv. Appl. Mech. 27, 83–151.

Tvergaard, V., Needleman, A., 1984. Analysis of the cup-cone fracture in a round tensile bar. Acta Metall. 32 (1), 157–169.

Xue, L., 2007a. Damage accumulation and fracture initiation in uncracked ductile solids subject to triaxial loading. Int. J. Solids Struct. 44 (16), 5163–5181.

Xue, L., 2007. Ductile Fracture Modeling – Theory, Experimental Investigation and Numerical Verification (Ph.D. thesis). SchoolMassachusetts Institute of Technology (MIT).

Xue, L., 2008. Constitutive modeling of void shearing effect in ductile fracture of porous materials. Eng. Fract. Mech. 75 (11), 3343–3366.

Xue, L., Wierzbicki, T., 2009. Numerical simulation of fracture mode transition in ductile plates. Int. J. Solids Struct. 46 (6), 1423–1435.